ACS APPLIED MATERIALS & INTERFACES

www.acsami.org

Research Article

Broadband, Angle- and Polarization-Invariant Antireflective and Absorbing Films by a Scalable Synthesis of Monodisperse Silicon Nanoparticles

Parker R. Wray,[+] Mohammad Ali Eslamisaray,[+] Gunnar M. Nelson, Ognjen Ilic, Uwe R. Kortshagen,* and Harry A. Atwater*

Cite This: *ACS Appl. Mater. Interfaces* 2022, 14, 23624−23636

Read Online

ACCESS | Metrics & More | Article Recommendations | Supporting Information

ABSTRACT: Optically induced magnetic resonances (OMRs) are highly tunable scattering states that cannot be reproduced in systems that only support electric resonances, such as in metals, lossy, or low-index materials. Despite offering unique scattering and coupling behavior, the study of OMRs in thin films has been limited by synthesis and simulation constraints. We report on the absorption and scattering response of OMR-based thin films composed of monodisperse crystalline silicon nanoparticles synthesized using a scalable nonthermal plasma growth technique and tractable simulation framework. The synthesis is solvent and ligand free, ensuring minimal contamination, and crystalline particles form with high yield and a narrow size distribution at close to room temperature. Using a scalable high-throughput deposition method, we deposit random particle films, without the need of a solid host matrix, showing near complete blackbody absorption at the collective OMR. This is achieved using 70% less material than an optimized antireflective-coated crystalline silicon thin film. The film exhibits strongly directional forward scattering with very low reflectivity, thus giving rise to angle- and polarization-insensitive antireflection properties across the visible spectrum. We find that, while commonly used effective medium models cannot capture the optical response, a modified effective medium accounting for multipole resonances and interparticle coupling shows excellent agreement with experiment. The effective permittivity and permeability are written in a mode and cluster resolved form, providing useful insight into how individual resonances and nanoparticle clusters affect the overall film response. Electric and magnetic-mode coupling show dramatically different behavior, resulting in uniquely different spectral broadening.

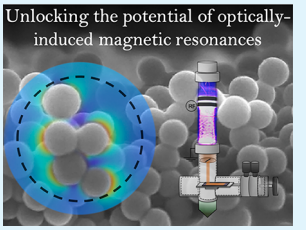

KEYWORDS: *antireflection, absorber, nanoparticles, nanocrystals, optical magnetic resonance, plasma, films*

INTRODUCTION

The Maxwell−Garnett and Bruggeman theories show that through the proper mixture of vanishingly small uncoupled particles, an inhomogeneous medium could give rise to optical phenomena not seen in homogeneous single-phase media.[1] Particle mixtures of this type spawned some of the first examples of metamaterials,[2] whose paradigm envision subwavelength, resonant -but independent and uncoupled- scatterers. For densely packed nanoparticles, there is a much broader set of emergent phenomena that occurs in *coupled Mie resonant* particles. Multiple works have shown that designing in this boarder space is indeed fruitful.[3−6] For example, optically induced *electric* resonances (OERs) excited by localized surface plasmons have shown rich resonant and coupling behavior in deeply subwavelength metallic particles.[7,8] The resulting confined local fields and sensitivity to particle size and shape further broadened the scope of applications, such as in the fields of energy, sensing, and more.[9−12] More recently, researchers have recognized the potential of optically induced *magnetic* resonances (OMRs), which are supported in subwavelength low-loss and high-index dielectric particles that enable access to scattering and absorption states not achievable in other particles, such as metals or low-index materials.[13−20] Correspondingly, crystalline semiconductors are target materials for producing OMRs in the visible and in particular, crystalline silicon (c-Si). The OMR arises from the creation of a strong circulating field *within the core* of the particle and can have a large quality factor. This resonance is spectrally tunable by particle size, exists in low-loss spectral regions, and has distinctly different behavior compared to OERs.[13,15,16,21−34] Therefore, OMRs offer the potential to further the applications of particle mixtures by expanding the state space and material library for achieving emergent phenomena. Despite the unique properties, most experimental research on OMR particles has been limited to single particle characterization or nanostructures synthesized by top-down lithographic techniques.[13,15,26−28] This is due to a synthesis

Received: February 21, 2022
Accepted: April 15, 2022
Published: May 12, 2022

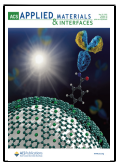

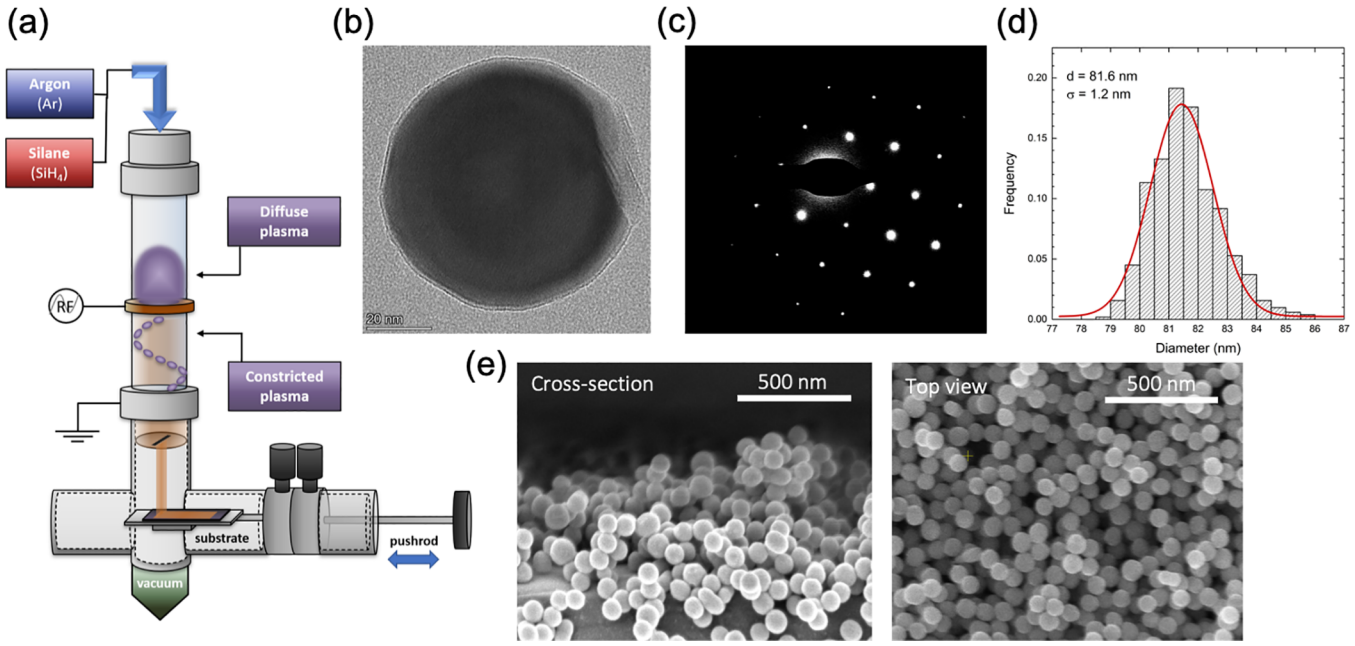

Figure 1. (a) Schematic of the flow-through nonthermal plasma reactor showing the diffuse and filamentary discharge regions. (b) Representative bright-field TEM image of a single nanocrystal synthesized in the reactor. (c) Electron diffraction pattern of a silicon nanocrystal aligned with the electron beam. (d) Size distribution of OMR supporting nanocrystals, showing an average diameter of 81.6 nm with a standard deviation of 1.2 nm. (e) Cross-sectional and top-down SEM image of the nanocrystal film deposited on glass with a fractal-like structure and an average thickness of 550 nm.

bottleneck arising from constraints in synthesizing crystalline semiconductor nanoparticles in the OMR regime (around 80 nm diameter). Furthermore, theoretical considerations of particle mixtures have largely neglected the existence of OMRs, which causes non-negligible inaccuracies in previously reported theories because of the strong resonant features and unique coupling behavior of the OMR.[1,35−38]

To explore further the potential of nanoparticle based effective media, we must advance our conceptual framework for the scattering and absorption response of nanoparticle films to allow for the features of OMRs. To address this, we report the synthesis and optical scattering and absorption characteristics of an angle and polarization-invariant resonant nanoparticle-based film reliant on the OMRs found in appropriately sized c-Si nanoparticles. The nanoparticles are fabricated using a dusty plasma synthesis technique capable of making highly monodispersed c-Si particles. By coupling a simple and scalable spray deposition method to the plasma nanoparticle synthesis, a fractal-like random film is formed in an air host matrix, which is particularly suited for making strong absorbers using little material.[39−44] To understand the resulting emergent behavior, we develop an effective medium theory which accounts for both the fractal-like film deposition and a complete representation of the coupled particle resonance characteristics. The OMR nanoparticle film scattering properties are shown to be dramatically different compared to both conventional planar film counterparts and predictions from classical effective medium theories.

Nonthermal plasmas are widely used for synthesis of covalently bonded groups IV and III−V semiconducting nanocrystals owing to their nonequilibrium environment which enables the nucleation, growth, and crystallization of high melting point materials from gas phase precursors at room temperature.[45−50] While in the plasma, particles above a certain minimum size are negatively charged,[51−53] which suppresses particle agglomeration.[54,55] Upon exiting the plasma, particles can be accelerated through a nozzle to form thin films via impaction onto a substrate.[56,57] The scalability of this single step, ligand-free, and high yield deposition technique has recently been demonstrated by Firth et al.[58] Nevertheless, the application of dusty plasmas has been limited to synthesis of small nanocrystals (mostly in a size range of 2 to 10 nm diameter), owing to the short residence time of particles in the plasma discharges. Bapat et al.[59] were the first to report the possibility of producing monodispersed Si nanocrystals of ∼35 nm by operating the synthesis plasma in a regime where the particle residence time in the plasma is extended through electrostatic particle trapping. Once particles leave the trap, they travel through a plasma zone in which the plasma is filamentary constricted. We expand this work to a new size regime using the same discharge concept to produce resonant Si nanocrystals of over 80 nm in diameter by the trapping mechanism and residence time.

The impaction deposition method produces random fractal-like films where each particle is connected to *at least one nearest neighbor* in an air host matrix.[39−44] Particle clusters can exhibit strong near-field coupling, leading to substantially increased absorption and antireflection, even in the limit of vanishing inclusion fill fraction.[39−44,60] Absorption at longer wavelengths comes as an added benefit to the creation of the shorter wavelength unit cell as long as the material and spatial statistical properties remain unchanged.[39] Therefore, the upper and lower spectral absorption limit is dictated by the inclusion (i.e., particle design) and cluster size, highlighting the desire to control both.[39]

In defining a homogenization scheme for such a film, it is important to account for particle effects traditionally assumed to be negligible, such as OMRs, and general higher-order excitations. Furthermore, the theory must account for properties unique to the fractal-like clusters which exhibit

https://doi.org/10.1021/acsami.2c03263
ACS Appl. Mater. Interfaces 2022, 14, 23624−23636

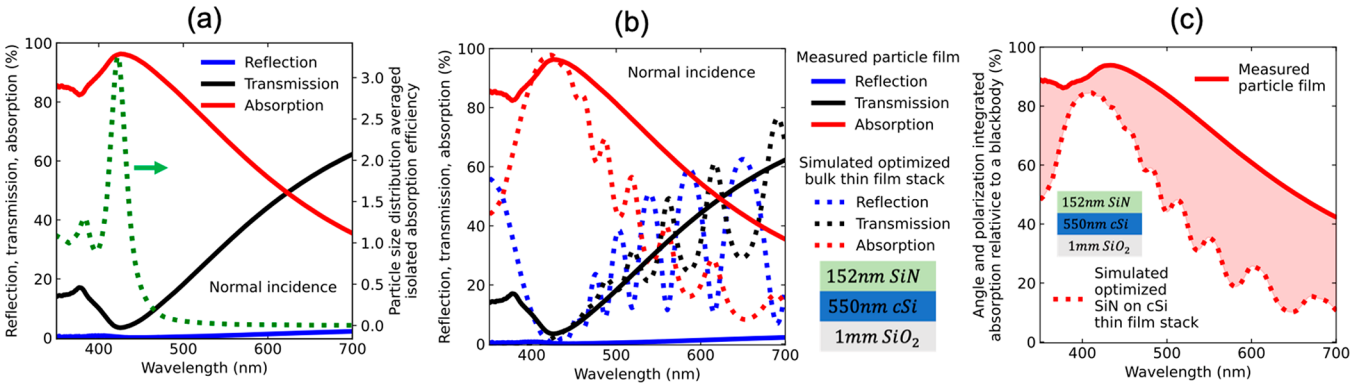

Figure 2. Comparison of the measured resonant nanoparticle film to an optimized homogeneous bulk thin film stack. (a) Measured transmission (black), reflection (blue), and absorption (red) response at normal incidence from a 550 nm thick particle film with a 30% volume fill fraction on 1 mm of soda-lime glass. The response is polarization averaged at an incident angle of 6 degrees. The green dashed curve and right *y*-axis plots the particle size averaged absorption efficiency of isolated c-Si particles in free-space, calculated using Mie theory. The average was weighted based on the particle size distribution given in Figure 1d. (b) Comparison of the transmission (black), reflection (blue), and absorption (red) response at normal incidence from the measured particle film (solid lines) to a simulated bulk homogeneous thin film stack of 152 nm SiN on 550 nm cSi on 1 mm of glass (botted lines). The bulk thin film stack was optimized to maximize absorption at 420 nm. (c) Angle and polarization integrated absorption relative to a perfect absorbing blackbody of the measured particle film (solid, red) and the simulated optimized bulk homogeneous thin film stack (red, dashed). The red shaded area highlights the absorption enhancement achieved when transitioning from a thin film to resonant particle-based absorber.

strong near-field coupling even at low fill fractions and lack long-range order.[43,61−66] This is exacerbated by the fact that OMR coupling is distinctly different from electric dipole coupling. Finally, it is also important to develop a theory which gives rise to a physical understanding of how these features shape the overall electromagnetic response. Parameter retrieval methods, such as S-parameter retrieval, can accurately model measured data but otherwise provides little physical insight.[67] We attempt to address these issues by formulating a parameter retrieval method based on the known physics of the constituent particles and deposition methods. The theory is built upon previous research relating particle multipoles to film-level effective induced electric and magnetic current densities.[68] However, their theory does not account for the coupling between OER particles, OMR particles, or between OERs and OMRs. Our primary contribution to expanding the homogenization approach is to propose a method to address this for the system stated above.

RESULTS AND DISCUSSION

Si nanocrystals that support OMRs were synthesized with an average size of 81.6 nm and a standard deviation of 1.2 nm via a nonthermal plasma process as described in detail elsewhere.[59,69] A schematic of the flow-through reactor used in this study is shown in Figure 1a. The primary gas feed, a mixture of silane and argon, enters through the top of the 38 mm-outer diameter glass reactor tube. A plasma is generated in the reactor tube by applying 200 W of radio frequency (RF) power at 13.56 MHz through a copper ring electrode. At low silane flow rates and high RF powers, the plasma operates in a regime where the discharge is constricted. In this regime, the plasma consists of two regions: a diffuse region that extends a few centimeters upstream of the RF electrode, and a striated, high-luminosity plasma filament that rotates close to the wall of the tube between the RF electrode and the lower grounded metal flange. Previous laser scattering studies[59] have shown that the particle formation begins in the diffuse plasma and particles are trapped in electrostatic potential traps formed upstream of the powered electrode. This trapping mechanism enables the growth of the initial amorphous nanoparticles to sizes as large as a few hundred nanometers. The filamentary plasma provides a significantly higher plasma density and, thus, sinters the particles by annealing them to temperatures much higher than the gas temperature resulting in formation of single crystals. Figure 1b shows a representative bright-field transmission electron microscope (TEM) image of a particle collected in the deposition chamber. The nanoparticle is nearly spherical, as suggested by the thickness fringes and can be verified by tilting the particles to different orientations. The particle is a single crystal as verified by the selected area diffraction pattern (Figure 1c). Figure 1d represents the nanoparticles highly monodisperse size distribution, obtained by image analysis of over 500 nanoparticles collected on TEM grids. The average particle size could be adjusted via changing the argon flow rate and therefore the particle residence time in the plasma reactor. The particle diameters in this study (between 79 and 86 nm) correspond to OMR spectral peaks from 417 to 433 nm, respectively. The particle size averaged OMR spectral peak is 420 nm, according to Mie theory. The spectral deviation of the OMRs as a function of particle size is considered negligible with respect to the spectral broadening effects of particle coupling (more detail below). Therefore, particles from this reactor can be regarded as supporting comparatively the same OMR. Random films of OMR-supporting particles are formed immediately downstream of the synthesis reactor via impaction of the nanocrystals onto the substrate.[57,58] Using this technique, we deposited an approximately 550 nm thick, random film with a 30% volume fill fraction on a 1 mm thick soda-lime glass substrate for optical characterization. The deposition parameters provide an optical thickness that exhibits near blackbody behavior at the OMR, discussed below, without losing characteristic spectral features from an overly large optical depth. This is necessary for understanding the physics behind the nanoparticle film scattering response. Figure 1e shows a representative top-view (left) and cross-sectional (right) scanning electron microscope (SEM) image of the film, showing a uniform coverage of particle clusters.

https://doi.org/10.1021/acsami.2c03263
ACS Appl. Mater. Interfaces 2022, 14, 23624−23636

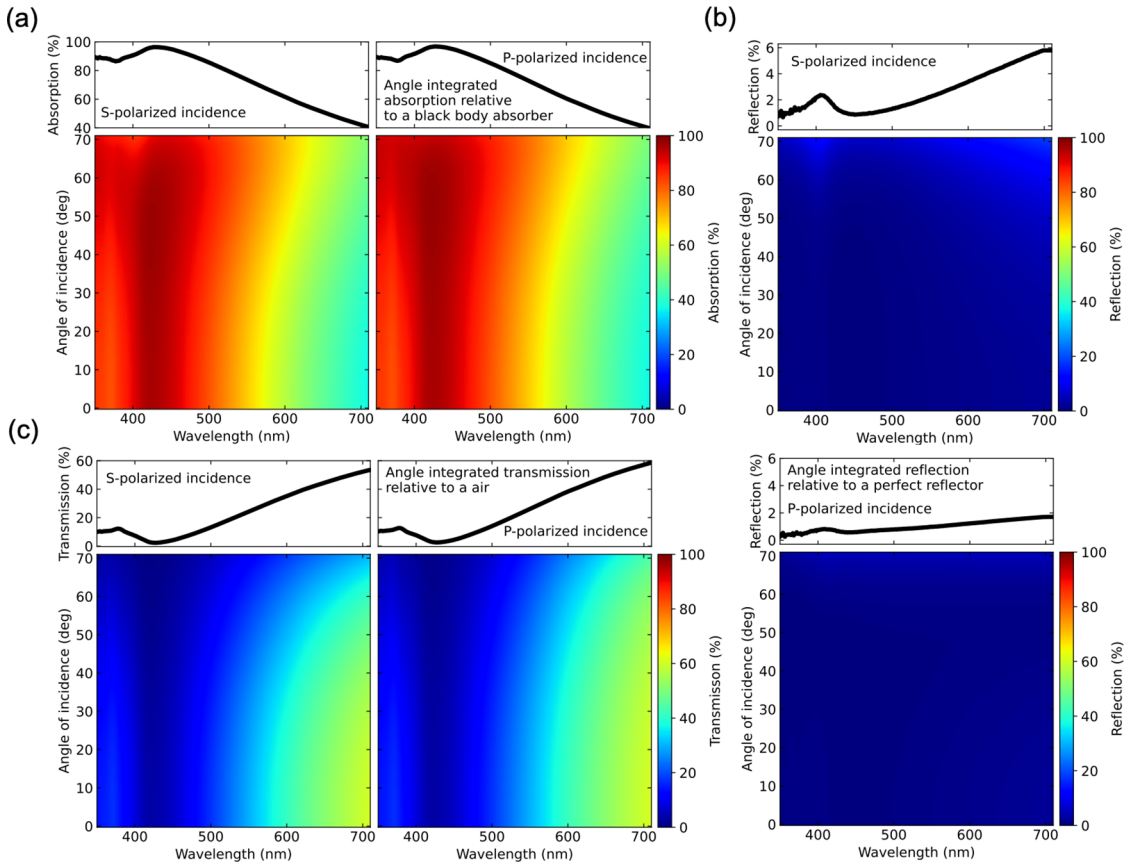

Figure 3. Angle, wavelength, and polarization resolved absorption, reflection, and transmission response of a 550 nm thick c-Si OMR supporting particle film on top of a 1 mm thick soda-lime glass substrate. (a) Bottom color maps show the film's absorption response as a function of wavelength (*x*-axis), angle of incidence (*y*-axis), and s- (left) and p-polarization (right). The corresponding top figures are the angle integrated absorption of the respective bottom color map, normalized to an ideal blackbody. (b) Reflection response of the particle film for s- (top) and p-polarization (bottom). In both cases the angle integrated reflection relative to a perfect reflection is shown above the corresponding color map. (c) Film's transmission response for s- (left) and p-polarization (right) with the angle integrated transmission relative to air shown above the respective color map.

To study the absorption and scattering response of this film, angle, polarization, and wavelength resolved reflection and transmission measurements of the film were taken using an Agilent Cary 5000 UV−vis−NIR with a Universal Measuring Attachment (UMA). Diffuse scattering was shown to be negligible (see the Supporting Information for more detail), so absorption was calculated as $A = 1 - R - T$, where R and T are the reflection and the transmission of the film, respectively. Figure 2a shows the film polarization averaged transmission (black), reflection (blue), and absorption (red) spectra near normal incidence (6 degrees). The film shows a clear absorption peak of 96% at the size distribution averaged particle OMR (420 nm) accompanied by a broadened absorption tail emanating from the OMR and progressing out to longer wavelengths. Interestingly, the absorption broadening is almost exclusively due to interparticle coupling altering the behavior of electric dipoles while the magnetic dipoles remain comparatively unchanged. This effect is discussed in detail later in this section. For now, we compare the absorption response of the film to uncoupled particles simulated using the Mie solution for a particle suspended in free space. Simulated nanoparticle sizes are based on the size distribution from Figure 1d and the size distribution averaged absorption efficiency is then overlaid as a reference (dashed green). The uncoupled particle absorption is clearly peaked at the OMR which is also consistent with the film's overall absorption peak. This supports the concept that the OMR remains intact in the particle film. The uncoupled particle absorption also shows substantially less spectral broadening at longer wavelengths with respect to the film. This supports the propensity for clusters to broaden absorption, which we later show is primarily an electric dipole effect. The film also has strikingly broadband antireflection everywhere below 2.2% at near normal incidence. This indicates almost complete coupling of the incident field leading to absorption limited by optical depth. Interestingly the antireflection is achieved despite the strong interactions between particles and the incident field. This is in direct contrast to the predictions of the Maxwell−Garnett and Bruggeman formulas, which predict antireflection, because of a weak interaction with the incident field. These results are further discussed when introducing the effective medium model later in this section.

To understand how this film compares to an optimized thin film equivalent, Figure 2b compares the absorption response of the measured particle film at normal incidence to that of a simulated dense homogeneous thin film stack that has been optimized using an antireflection (AR) layer to maximize absorption centered at 420 nm. The thin film stack is composed of 152 nm thick silicon nitride (SiN) on top of 550 nm c-Si on a 1 mm glass substrate. We find that though

https://doi.org/10.1021/acsami.2c03263
ACS Appl. Mater. Interfaces 2022, 14, 23624−23636

the thin film stack can be optimized to mimic the absorption peak at 420 nm, it cannot mimic the spectral broadening in absorption. Furthermore, the antireflection of the thin film stack is less broadband and overall around 10× worse compared to the particle film when averaged over the measured spectral range. Figure 2c integrates the angle and polarization absorption response of both the measured particle film (solid red) and optimized thin film stack (dotted red). The overall absorption is then normalized to that of an ideal blackbody. Comparing the entire polarization, angle, and specular range, the particle film is over 38% more absorbing than a c-Si slab of the same thickness; even after enhancing the c-Si slab absorption by adding an optimized SiN coating on top. Furthermore, the enhanced performance in absorption of the particle film is accomplished using 70% less Si than the thin-film counterpart, does not require a top coating, and is overall 78% lighter compared to the thin film stack.

To understand the effect of polarization and angle dependence, Figure 3 plots the measured angle, polarization, and wavelength resolved absorption, reflection, and transmission response of the particle film. Similar to a blackbody, Figure 3a shows near complete absorption at the OMR with strong angle insensitivity up to angles of incidence as steep as 70 degrees and almost no change in behavior as a function of incident polarization. The top two plots in Figure 3a show the angle integrated absorption of the nanoparticle film relative to a blackbody over the same angular and spectral range. At the OMR, the nanoparticle film absorption reaches 96% of the absorption of an ideal blackbody. Figure 3b shows the particle film has antireflective properties for both polarizations. The film also shows no well-defined Brewster angle and only slight polarization splitting at large incident angles. The particle film's absorption is optical depth-limited throughout the measured spectral range, as evident by the fact that $T \approx 1 - A$ (Figure 3c).

Given negligible scattering pathways, the film's response can be described by a homogenized field coherent to the specular direction. Thus, a properly chosen effective medium can be used to generate a valid description of the optical response through the transfer-matrix method. The goal of our proposed effective medium method is to accurately model the experimental data in Figure 3 using known film properties from Figure 1. Furthermore, the method is intended to provide insight into how particle coupling behavior dictates the film's optical behavior. This includes the effect of variations in local particle density, interparticle coupling, and the differences between electric and magnetic-type multipole coupling. Our approach generalizes the framework previously outlined[68] to account for particle coupling and leverages the result that coupling effects in a fractal-like film are localized to clusters that are otherwise electromagnetically topologically disconnected.[39−41] Our overall concept is that coupled particles create effective particles, which then create effective media. Cluster distributions are first simulated using a Monte Carlo event-driven 3D particle aggregation model. The goal of this model is to accurately represent the particle packing behavior that characterizes the fractal-like aggregates generated using the spray method described above. This approach has been well studied for accurately modeling films of this type.[70−72] The particle sticking coefficient, which scales the probability a particle will stick to another particle when coming into contact, was determined by ensuring the average volume fill fraction of 100 sampled clusters, with the same radii distribution as shown in Figure 1d, matched the experimental value of 30%. We found cluster sizes varying from 4 to 20 particles with equal probability provided a good fit to the experimental data and use the sampled cluster distribution to study how local variations in packing fraction and cluster size impacts the overall film response. Consistent with the definition that a homogenized field is the particle orientation averaged electromagnetic response of the film, our effective medium is ultimately determined by the Monte Carlo integration of samples to find the average of the electromagnetic response from each cluster. Therefore, the dependence on sample number can be quantified by the uncertainty in the sample mean and convergence to the true homogenized film is guaranteed. The Supporting Information shows 100 samples was sufficient to accurately reproduce the data in Figure 3. Once clusters are generated, their electromagnetic response is simulated under plane wave excitation using the extended boundary technique; also known as the null-field method or generalized Mie theory.[16,73−76] Plane wave excitation is consistent with particle clusters being uncoupled[68] and is analogous to clusters interacting only with the incident excitation under the scattered field formalism. Using generalized Mie theory to solve the coupling problem allows for an exact solution, meaning all coupling effects within the cluster are properly represented.[76,77] This approach is analytical, provides an intuitive definition of particle-driven electromagnetic behavior as atom-like multipoles, and can be between 1 and 2 orders of magnitude computationally faster compared to full-wave techniques.[16,76,78−80] The overall electromagnetic response of a cluster is then transformed into a single expansion of multipoles that completely accounts for the collective behavior of all particles within the cluster, including interparticle coupling. Once transformed into a single expansion, the collective response can be viewed as coming from an "effective particle". This provides a method of studying the overall cluster's electromagnetic properties in terms of multipoles which are driven by the collective as opposed to single particle multipoles inside of the collective. Under this framework, we can study how individual particle resonances dictate the resulting collective behavior. The transform is done by re-expanding the multipole solution of each individual particle in a cluster about the cluster center, using the addition theorem for spherical harmonics.[76,77] After each sampled cluster is written as an effective particle, the effective permittivity and permeability can be written, in terms of the effective particles, in a form that is parametrized by incident polarization (ν), cluster sample number (l), cluster multipole order (n), and cluster multipole type (magnetic, p = 0, or electric, p = 1). This is expressed in compact notation as

https://doi.org/10.1021/acsami.2c03263
ACS Appl. Mater. Interfaces 2022, 14, 23624−23636

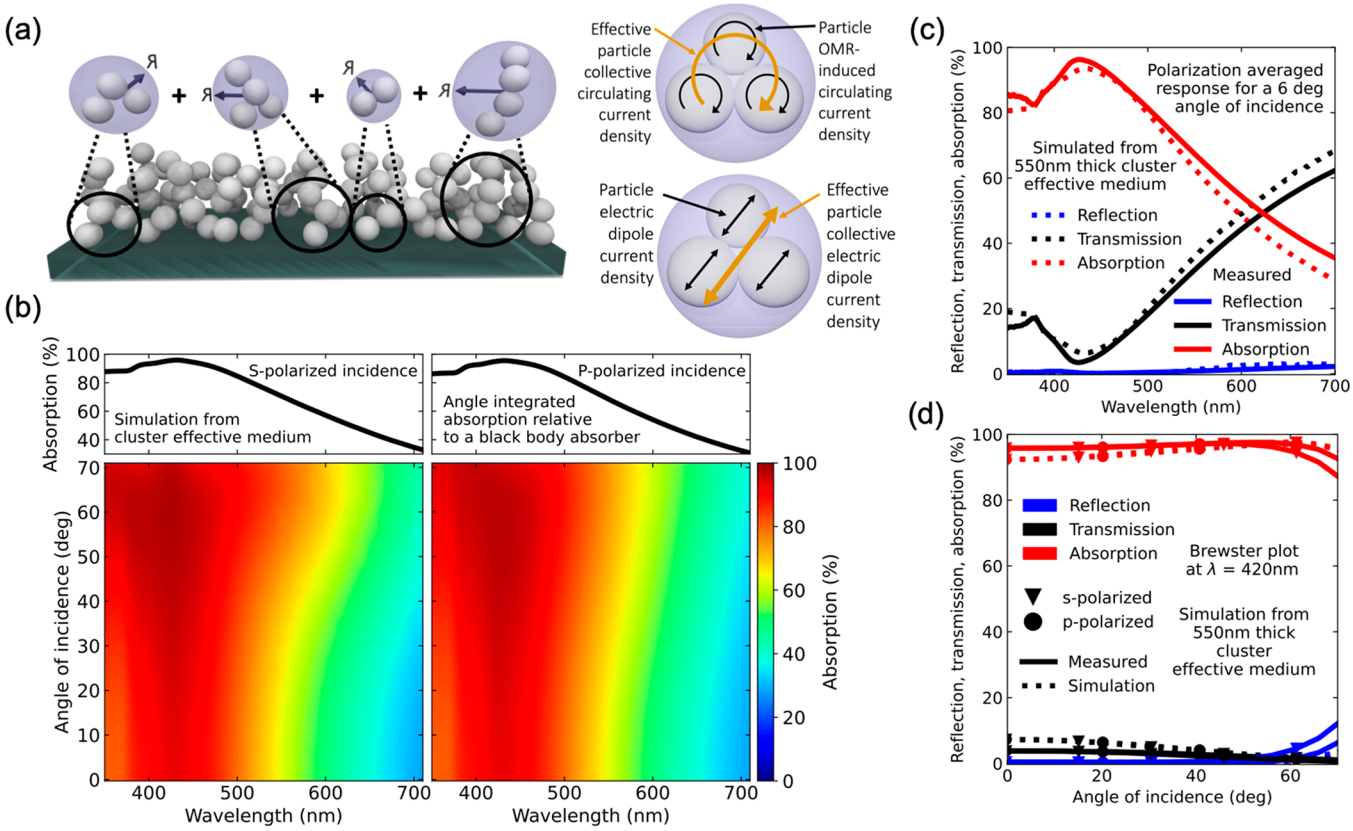

Figure 4. Comparison of the measured absorption, reflection, and transmission from Figure 2 to the calculated response from the transfer matrix method, using the proposed cluster-based effective medium. (a) Pictorial description for calculating the effective medium by simulating particle clusters, then representing them as effective uncoupled particles in a random film. (b) Analogous color map to the one shown in Figure 3a, but for the simulated film's response. (c) Polarization averaged absorption (red), reflection (blue), and transmission (black) spectral response at 6 degrees incidence of the simulated film (dashed) and measurement (solid). (d) Brewster plot of the absorption (red), reflection (blue), and transmission (black) response at the OMR resonance (λ = 420 nm) for the simulated film (dashed) and measurement (solid). s- and p-polarization are denoted with a downward triangle and circle marker, respectively.

$$
\begin{aligned}
\epsilon^{\mathrm{TE}}_{\mathrm{eff},lnp}(\theta_i) &= \frac{1}{2LN} + \frac{i\gamma_l}{L}\sum_{m=0}^{n} c^{\mathrm{TE}}_{\mathrm{sca},l,nmp} \\
&\quad (\mathbb{t}^{+}_{nmp}(\theta_i) - \tan^2(\theta_i)\mathbb{t}^{-}_{nmp}(\theta_i)) \\
\epsilon^{\mathrm{TM}}_{\mathrm{eff},lnp}(\theta_i) &= \frac{1}{2LN} + \frac{i\gamma_l}{L}\sum_{m=0}^{n} c^{\mathrm{TM}}_{\mathrm{sca},l,nmp}\frac{\mathbb{t}^{-}_{nm(1-p)}(\theta_i)}{\cos^2(\theta_i)} \\
\mu^{\mathrm{TE}}_{\mathrm{eff},lnp}(\theta_i) &= \frac{1}{2LN} + \frac{i\gamma_l}{L}\sum_{m=0}^{n} c^{\mathrm{TE}}_{\mathrm{sca},l,nmp}\frac{\mathbb{t}^{-}_{nmp}(\theta_i)}{\cos^2(\theta_i)} \\
\mu^{\mathrm{TM}}_{\mathrm{eff},lnp}(\theta_i) &= \frac{1}{2LN} + \frac{i\gamma_l}{L}\sum_{m=0}^{n} c^{\mathrm{TM}}_{\mathrm{sca},l,nmp} \\
&\quad (\mathbb{t}^{+}_{nm(1-p)}(\theta_i) - \tan^2(\theta_i)\mathbb{t}^{-}_{nm(1-p)}(\theta_i))
\end{aligned}
\tag{1}
$$

where $c^{\nu}_{\mathrm{sca},nmp}$ is the effective particle's complex scattering coefficient, L is the total number of samples, and N is the largest multipole supported by the cluster. The incident field's polarization is written explicitly where ν = TE denotes transverse-electric polarization and ν = TM denotes transverse-magnetic polarization. The angle of incidence is θ_i. $\gamma_l = \frac{\mathrm{ff}_l}{\frac{2}{3}x_l^3}$ is weight factor for the lth effective particle, that is based on that cluster's inclusion volume fill fraction (ff_l) and size parameter ($x_l = kr_l$). Here, r_l is the radius of the smallest circumscribing sphere encapsulating all particles in the cluster and $k = 2\pi/\lambda$ is the free space wavenumber. Therefore, the weight factor can be used as a measure of a cluster's geometric properties that also has relevance to the cluster electromagnetic response. The basis function, $\mathbb{t}^{\pm}_{nmp}(\theta_i) = \tau_{nmp}(0) \pm \tau_{nmp}(\pi - 2\theta_i)$, is a superposition of the Mie polar angle functions, $\tau_{nmp}(\theta_i)$, and describes the angular dependence of the film permittivity and permeability based on an effective particle multipole mode order and type. The total effective permittivity and permeability can then be written by superposition as $\epsilon^{\nu}_{\mathrm{eff}} = \sum_l \sum_n \sum_p \epsilon^{\nu}_{\mathrm{eff},lnp}$ and $\mu^{\nu}_{\mathrm{eff}} = \sum_l \sum_n \sum_p \mu^{\nu}_{\mathrm{eff},lnp}$. Further detail about deriving the generalized Mie solution and the effective medium approach described above can be found in the Supporting Information. The ability to linearly decompose the permittivity and permeability into components associated with cluster type, mode order, and mode type is a notable benefit of this method, providing a tractable approach for describing and understanding how these variables give rise to the overall response. Finally, the effective medium is used to simulate the particle film's reflection, transmission, and absorption response using the transfer matrix method; accounting for nonunity permeability.[81]

A schematic of how the effective medium is formed based on the method described above is shown in Figure 4a. The

https://doi.org/10.1021/acsami.2c03263
ACS Appl. Mater. Interfaces 2022, 14, 23624−23636

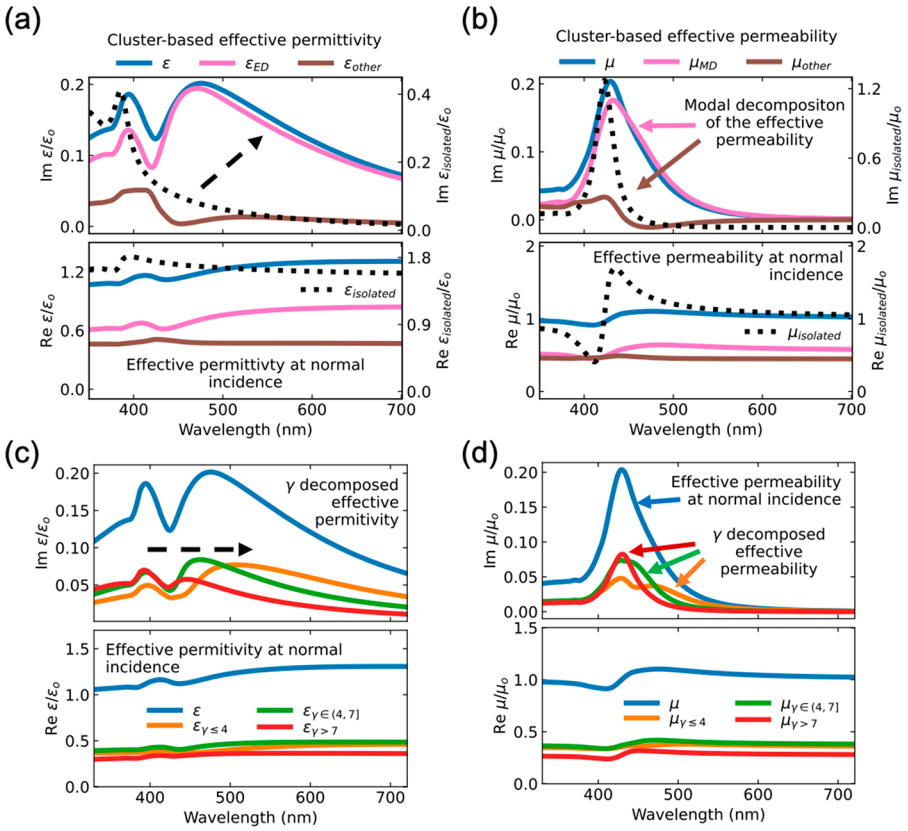

Figure 5. Analysis of the simulated cluster-based effective relative permittivity and permeability as a function of mode order, *n*, and scale parameter, *γ*. (a) Decomposition of the film's effective permittivity (blue) into the contribution from the electric-dipole mode (pink) and all other modes (brown). The effective permittivity assuming uncoupled particles that are homogeneously dispersed in air (dotted, black) is overlaid for reference. The black dashed arrow highlights spectral broadening when transitioning from an uncoupled particle film to a clustered film. (b) Decomposition of the film's effective permeability (blue) into the contribution from the magnetic-dipole mode (pink) and all other modes (brown). The effective permeability assuming uncoupled particles (dotted, black) is overlaid for reference. In both panels a and b, cluster-based values are measured based on the left *y*-axis and uncoupled values are measured according to the right *y*-axis. The respective scales are different to more clearly compare spectral shape. (c) Decomposition of the film's effective permittivity (blue) into the response from clusters with scale parameters above 7 (red), between 4 to 7 (green), and below 4 (orange). The black dashed arrow outlines the trend of absorption broadening and red-shifting as a function of decreasing scale parameter. (d) Decomposition of the film's effective permeability based on the same scale parameter ranges as in panel c. In all cases, the imaginary part of the complex relative permittivity or permeability is the top figure. The real part is the bottom figure.

modeled effective medium film was 550 nm thick on a 1 mm glass substrate. Thickness was determined from cross-sectional SEM images of the measured particle film. Figure 4b shows the angle, polarization, and wavelength resolved absorption of the simulated film. Comparing this to the measured data in Figure 3a, strong agreement is seen indicating the ability to represent the response of the measured film under all input excitations. Corresponding plots for reflection and transmission are shown in the Supporting Information and show agreement with experimental data in Figure 3b and 3c, respectively. Figure 4c shows the resulting polarization averaged reflection, transmission, and absorption response from simulation (dashed) compared to the measured data (solid) at 6 degrees incidence. We see good agreement throughout the entire spectral range showing the ability to properly represent both the OMR spectral peak and the resulting broadening emanating from that resonance. Reflection and transmission curves confirm an optical depth limited system. Figure 4d is a Brewster plot at the OMR demonstrating that the effective medium agrees with measurements, including the lack of a well-defined Brewster effect and minimal polarization splitting.

To further understand how particle resonances and interparticle coupling dictate the effective medium response, Figure 5 plots the effective permittivity and permeability at normal incidence. The constitutive parameters are then decomposed in terms of mode order and cluster weight. Figure 5a shows that the particle film's effective permittivity (blue) is primarily a result of the first-order electric dipole (ED) mode (orange) present in the effective particles, with a small contribution from all other terms (green). The spectral shape of the collective ED clearly shows that its spectra is sensitive to interparticle coupling. To show how the response is different compared to a uniform dispersion of uncoupled particles, we overlay the effective permittivity according to the original method (dashed black), which does not account for particle coupling.[68] The full width at half maximum of the imaginary part of the cluster-based effective permittivity encompasses 65% of the spectral range, whereas the uniformly dispersed and uncoupled particle case encompasses only 16% of the spectral range. The peak of the imaginary part in the cluster-based effective permittivity is also approximately half of the uncoupled counterpart, leading to broadband antireflection. This reduction is a direct consequence of energy balance. When coupling is neglected, the energy extracted from the incident field is nonphysical and overcounted because of the assumption of nonoverlapping cross sections between

https://doi.org/10.1021/acsami.2c03263
ACS Appl. Mater. Interfaces 2022, 14, 23624−23636

particles. In reality the clustered film has significant overlapping cross sections and near-field coupling transfers the energy between particles.[16,82] Figure 5b shows that the particle film's effective permeability (blue) is composed primarily of the first-order magnetic dipole (orange) with the contribution from other terms shown in green. The first-order magnetic dipole is an OMR excited *in the sampled effective particles*. This means the individual excitations of coherently coupled particles within a cluster are working together to create a strong *collective* OMR. An illustration of this effect is shown on the right-hand side of Figure 4a. We can interpret the circulating fields from the effective particles' OMR as a circulating current density in the film creating an induced magnetization.[32,68] The permeability of uncoupled OMR particles is shown as a reference (dotted, black). Interparticle coupling creates a staggering 6-fold reduction in the peak imaginary permeability, compared to the uncoupled counterpart. This is primarily because the uncoupled particle has an OMR with an optical cross-section that is much larger than the particle's geometric cross-section. To understand better how the collective ED is shaped through interparticle coupling, Figure 5c decomposes the effective permittivity based on cluster weight factor. Three distinct regimes of spectral broadening are identified and shown to be associated with cluster size. The regimes are large clusters of 15−20 particles ($\gamma_l \leq 4$, orange), to midsize clusters of 10−15 particles ($4 < \gamma_l \leq 7$, green), to smaller clusters of 4−9 particles ($\gamma_l > 7$, red). The small dense clusters most closely maintain the spectral features of uncoupled particles. Progressing to larger particle chains leads to absorption broadening and red shifting of the absorption resonance, as shown by the dashed black arrow. Figure 5d decomposes the effective permeability based on cluster weight factor, using the same three regimes as Figure 5c. We see the same trend of a reduced amplitude and red-shifted resonance with increasing cluster weight; though the effect is substantially less pronounced. This further affirms that OMR for each nanoparticle is robust to coupling-induced changes in spectral features.

Next, we study how interparticle coupling alters the modal response of individual particles within the effective particles that make up the particle film. Figure 6 compares the magnitude of the magnetic and electric dipole modes of uncoupled particles (top left and right, respectively) to that of particles within the sampled clusters (bottom left and right, respectively). The modal response for an individual uncoupled particle was calculated using the Mie solution to a single particle suspended in free space and far away from any other inhomogeneity. As detailed above, the modal response of a particle in a sampled cluster is found using generalized Mie theory. The solution for each particle is then expanded about the cluster's origin. This technique allows for an effective particle modal response to be described by the coherent superposition of the modes from the re-expanded individual particles making up the cluster. This enables a direct study on how each individual particle affects the effective particle response. In all cases, the mode magnitudes are shown as a function of wavelength on the *x*-axis and are ordered according to particle size on the *y*-axis. The color scale plots the mode magnitude normalized to the particle's size parameter. The magnetic dipole mode in each coupled particle clearly maintains a similar spectral shape to the uncoupled counterpart with the same radius. When comparing the coupled and uncoupled responses, a similar trend can be seen in terms of

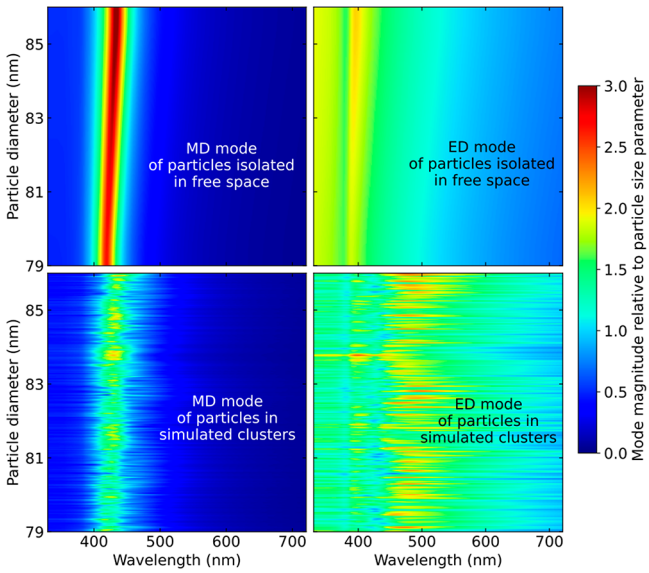

Figure 6. Comparison of uncoupled particles isolated in free space (top), magnetic-dipole (MD, left), and electric-dipole (ED, right) modes versus the same modes for particles in the simulated clusters (bottom), which are altered by interparticle coupling. In all cases, the *x*-axis is wavelength, and the *y*-axis is particle diameter.

spectral shift and average magnitude with increasing particle size. On the other hand, the electric dipole mode of each coupled particle is substantially altered by the effect of interparticle coupling on the single particle level. The spectral shape of the coupled electric dipole mode is substantially broadened with little resemblance to the uncoupled counterpart; showing no clear spectral trend as a function of particle size. The drastic difference between the electric and magnetic dipole modes as a result of interparticle coupling clearly shows models which only consider the film from the viewpoint of pure dipole expansion neglect how the dipoles are generated in the first place.

To emphasize the accuracy of this model compared to other techniques, Figure 7 presents the effective medium calculations from the commonly used Maxwell−Garnett and Bruggeman effective medium theories. Figure 7a and 7c presents the polarization, angle, and wavelength resolved absorption of the particle film calculated from the Maxwell−Garnett and Bruggeman effective medium theories, respectively. Though our experimental film invalidates the stated assumptions of these two theories (i.e., there is strong interparticle coupling of multipole resonant particles in the experimental film), their ease of use, prevalence in literature, and consistent track record of accurately modeling data warrants a comparison to justify the admittedly more complicated approach proposed in this manuscript. As evident in the Figure 7a and 7c, instead of blackbody-like behavior as seen in the measurement results, the Bruggeman and Maxwell−Garnett theories predict little absorption and are instead mostly transparent (see the Supporting Information). This is because these theories do not account for resonant behavior such as a strong OMR or interparticle coupling. This is further evident in the fact that neither theory accounts for a change in relative permeability that is necessarily generated by an optically induced magnetic response. Comparing the models to experiment, the relative difference in absorption is 180% (Bruggeman) and 680% (Maxwell−Garnett), when considering all angles, polarization,

https://doi.org/10.1021/acsami.2c03263
ACS Appl. Mater. Interfaces 2022, 14, 23624−23636

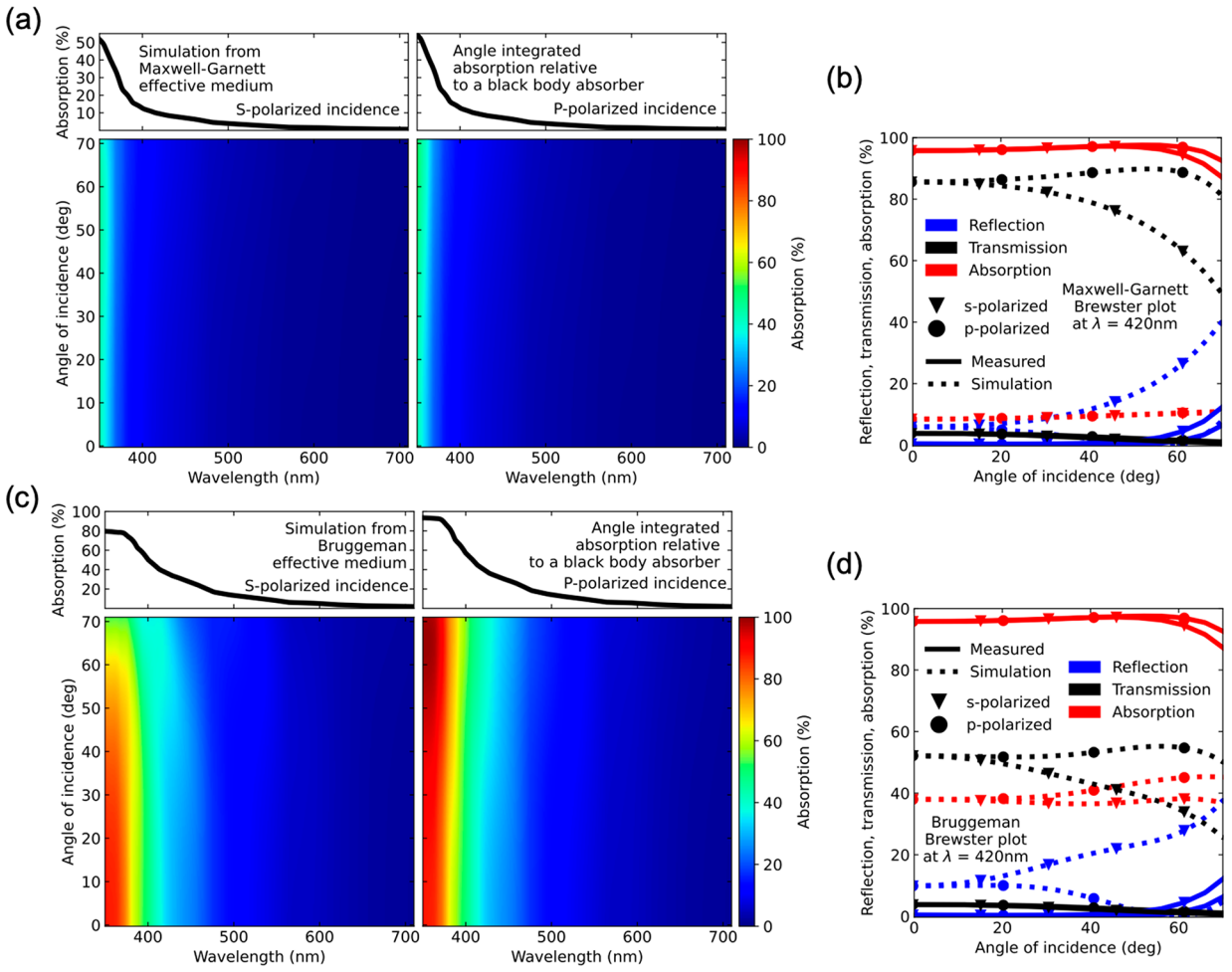

Figure 7. Angle, wavelength, and polarization resolved absorption response from a 550 nm thick effective medium on 1 mm soda-lime glass, calculated using the transfer matrix method. (a) Absorption response based on the particle film represented through the Maxwell−Garnett effective medium approach. (b) Brewster angle plot at λ = 420 nm of the measured reflection (solid blue), transmission (solid black) and absorption (solid red) response compared to the Maxwell−Garnett reflection (dashed blue), transmission (dashed black), and absorption (dashed red) response. The downward triangle and circle denote s- and p-polarization, respectively. (c) Absorption response based on the particle film represented through the Bruggeman effective medium approach. (d) Brewster angle plot at λ = 420 nm of the measured data compared to the Bruggeman effective medium. In both cases of the color maps, the angle (y-axis) and wavelength (x-axis) resolved absorption for s- (left) and p-polarization (right). The figure on top of each color map is the angle integrated absorption of the color map relative to an ideal blackbody.

and wavelengths. This is in stark contrast to the cluster-based method, which has a 6% relative difference in absorption when comparing to the experimental data. The relative difference is calculated using the formula, (experimental−simulation)/simulation. The Bruggeman and Maxwell−Garnett theories show no OMR absorption peak. Furthermore, both theories predict polarization splitting and a well-defined Brewster's angle where the OMR should exist, despite neither phenomenon present in experiment at that wavelength (λ = 420 nm). The polarization and angle dependence of the Maxwell−Garnett and Bruggeman theories are shown in the Figure 7b and 7d, respectively.

CONCLUSION

We have employed a dusty-plasma synthesis technique to make highly crystalline silicon nanoparticle films comprised of OMR particles. The process uses particle trapping and subsequent annealing in a high-density filamentary plasma and achieves highly monodisperse nanocrystals in the size range required to exhibit OMR. The particle size distribution is narrow enough such that all particles exhibit an average OMR at 420 nm with a negligible deviation compared to the spectral broadening from the electric dipole mode. Particles are then directly deposited onto a substrate from the reactor using a scalable spray method. The resulting particle film shows broadband angle and polarization independent antireflection across the visible spectrum as well as strong absorption emanating from the designed OMR. Since OMRs and near field coupling are neglected in traditional effective medium theories, we develop an analytical approach which accurately models the behavior of the experimental film. The model describes the film in terms of the scattering response of individual particles, and also gives an overall resulting effective permeability and permittivity. Furthermore, the effective constitutive parameters can be resolved by mode and cluster-type. We find the individual particle OMRs give rise to a collective OMR which, from the perspective of the film, can be viewed as a true magnetic response. Therefore, the film has a nonunity relative permeability despite being composed of nonmagnetic materials. The collective OMR is slightly red-shifted compared to uncoupled particles in free space, but the spectral shape is virtually unchanged by near field coupling. Studying coupling

https://doi.org/10.1021/acsami.2c03263
ACS Appl. Mater. Interfaces 2022, 14, 23624−23636

effects on the particle level shows the OMR in each particle is individually robust to interparticle coupling. In contrast, the electric resonance has substantial spectral broadening to longer wavelengths and is responsible for a majority of the absorption broadening within the film. Both resonances experience a reduction in amplitude on the particle-level to satisfy energy balance, leading to broadband antireflection. Maxwell−Garnett and Bruggeman effective medium theories cannot accurately account for the film scattering response. Furthermore, accounting only for uncoupled particle resonances resulted in constitutive parameters that were roughly double the appropriate amplitude and had 49% less spectral broadening than necessary, measured by the full width at half maximum. This indicates that both near-field coupling and individual particle resonances need to be considered.

METHODS

Nanoparticle Synthesis. Silicon nanocrystals are synthesized in a continuous-flow, low-pressure plasma reactor consisting of a quartz tube with an inner diameter of 3.5 and 20 cm long. Pure silane and argon enter through the top of the reactor with typical flow rates of 0.2 and 7.5 standard cubic centimeters per minute (sccm), respectively, leading to a gas residence time in the plasma zone of about 2 s. However, because of the electrostatic trapping of particles upstream of the ring electrode that was observed in ref 59 the actual particle residence time in the reactor is expected to be longer. The electrostatic trapping requires that particles grow to a minimum threshold size before being removed from the trap by the gas flow, which causes a size filtering of the particles, leading to a narrow size distribution.[83] The plasma is excited by applying a nominal radiofrequency (RF) power of 200 W at 13.56 MHz to a ring electrode placed 6.5 cm upstream of the lower flange, which serves as the ground electrode. Nanocrystals are extracted by the gas flow through a 12 × 0.064 mm slit-shaped orifice and injected into the deposition chamber. The typical pressure in the plasma reactor is 1.7 Torr while the deposition chamber downstream of the extraction orifice has a pressure of 80 mTorr. The nanocrystals are collected directly onto glass substrates located 1.5 cm beneath the orifice. To form homogeneous films, substrates are mounted on a stainless-steel pushrod setup and translated back and forth for 30 min.

Transmission Electron Microscopy. TEM samples were collected on thin holey carbon coated Cu grids. Conventional TEM examination of the nanocrystals was carried out using an FEI Tecnai T12 operating at an accelerating voltage of 120 kV to obtain the particle distribution size. High-resolution imaging was performed using an FEI Talos F200x operating at an accelerating voltage of 200 kV.

Scanning Electron Microscopy. The nanocrystal film thickness was approximated using cross sectional scanning electron microscopy. Specifically, an FEI Helios NanoLab G4 was used with an accelerating voltage of 2 kV.

UV−Visible Spectroscopy. Angle and polarization-resolved absorption data from 350 to 700 nm was acquired using Agilent Cary 5000 UV−vis−NIR with the Universal Measuring Attachment (UMA). Samples were angled from 6−71 degrees in 5 degree increments with respect to normal incidence from the lamp source. For specular reflection, the detector was angled at 2× the sample angle measured clockwise from the lamp source. Spectral transmission measurements required only the change of the sample angle, and the detector did not move from 180° from the incident light. All measurements were performed for both S and P polarizations. The schematic of the UV−vis measurement process is presented in the Supporting Information.

Fill Fraction Calculation. The mass of the sample was measured with a Cahn C-31 Microbalance. Density of the thin film was calculated using the sample area (4.5 mm × 10 mm), the measured film thickness from cross-sectional SEM (550 nm), and the mass of the nanocrystal film (17.4 μg). The volume fill fraction of the thin film (30%) was then determined as the ratio of the film density to bulk silicon density (2.329 g/cm^3).

ASSOCIATED CONTENT

Supporting Information

The Supporting Information is available free of charge at https://pubs.acs.org/doi/10.1021/acsami.2c03263.

Additional detail about calculating effective particles from a cluster of particles and deriving the cluster-based effective medium, angle and polarization resolved reflection and transmission of the cluster-based, Maxwell−Garnett, and Bruggeman effective medium films, and negligible diffuse scattering from the measured sample (PDF)

AUTHOR INFORMATION

Corresponding Authors

Uwe R. Kortshagen − *Department of Mechanical Engineering, University of Minnesota, Minneapolis, Minnesota 55455, United States;* orcid.org/0000-0001-5944-3656; Email: kortshagen@umn.edu

Harry A. Atwater − *Thomas J. Watson Laboratories of Applied Physics, California Institute of Technology, Pasadena, California 91125, United States;* orcid.org/0000-0001-9435-0201; Email: haa@caltech.edu

Authors

Parker R. Wray − *Department of Electrical Engineering, California Institute of Technology, Pasadena, California 91125, United States;* orcid.org/0000-0003-3384-0826

Mohammad Ali Eslamisaray − *Department of Mechanical Engineering, University of Minnesota, Minneapolis, Minnesota 55455, United States;* orcid.org/0000-0001-8704-592X

Gunnar M. Nelson − *Department of Chemical Engineering and Materials Science, University of Minnesota, Minneapolis, Minnesota 55455, United States*

Ognjen Ilic − *Department of Mechanical Engineering, University of Minnesota, Minneapolis, Minnesota 55455, United States*

Complete contact information is available at: https://pubs.acs.org/10.1021/acsami.2c03263

Author Contributions

[+]P.R.W. and M.A.E. contributed equally. P.R.W. conceived the idea, designed the experiments, developed the effective medium theory, and performed calculations, analysis, and interpretation of results pertaining to the electromagnetic aspects of the project. M.A.E. designed the nonthermal plasma reactor for nanoparticle synthesis and film deposition, and performed TEM for characterization of particle size, shape, and crystallinity. G.M.N. performed optical measurements of the particle film with oversight by P.R.W. and, with help from M.A.E., performed SEM and density calculations to determine the particle film's fill fraction and structure. H.A.A., U.R.K., and O.I. oversaw the project. All authors contributed to writing and editing the manuscript.

Notes

The authors declare no competing financial interest.

https://doi.org/10.1021/acsami.2c03263
ACS Appl. Mater. Interfaces 2022, 14, 23624−23636

■ ACKNOWLEDGMENTS

This work is supported by the Army Research Office under MURI project under W911NF-18-1-0240. Portions of this work were conducted in the Minnesota Nano Center, which is supported by the National Science Foundation through the National Nanotechnology Coordinated Infrastructure (NNCI) under Award Number ECCS-2025124. O.I. also acknowledges support from the 3M Foundation through the 3M Non-Tenured Faculty Award grant.

■ REFERENCES

(1) Choy, T. C. *Effective Medium Theory: Principles and Applications*; International Series of Monographs on Physics; Clarendon Press, 1999.
(2) Ziolkowski, R. W. Metamaterials: The Early Years in the USA. *EPJ. Applied Metamaterials* **2014**, *1*, 5.
(3) Zhai, Y.; Ma, Y.; David, S. N.; Zhao, D.; Lou, R.; Tan, G.; Yang, R.; Yin, X. Scalable-Manufactured Randomized Glass-Polymer Hybrid Metamaterial for Daytime Radiative Cooling. *Science* **2017**, *355* (6329), 1062−1066.
(4) Hsu, C. W.; Zhen, B.; Qiu, W.; Shapira, O.; DeLacy, B. G.; Joannopoulos, J. D.; Soljačić, M. Transparent Displays Enabled by Resonant Nanoparticle Scattering. *Nat. Commun.* **2014**, *5* (1), 3152.
(5) Capretti, A.; Lesage, A.; Gregorkiewicz, T. Integrating Quantum Dots and Dielectric Mie Resonators: A Hierarchical Metamaterial Inheriting the Best of Both. *ACS Photonics* **2017**, *4* (9), 2187−2196.
(6) Kim, H.; Chang, J. H. Increased Light Penetration Due to Ultrasound-Induced Air Bubbles in Optical Scattering Media. *Sci. Rep* **2017**, *7* (1), 16105.
(7) Kik, P. G.; Brongersma, M. L. Surface Plasmon Nanophotonics. In *Surface Plasmon Nanophotonics*; Brongersma, M. L., Kik, P. G., Eds.; Springer Series in Optical Sciences; Springer: Dordrecht, the Netherlands, 2007; pp 1−9. DOI: 10.1007/978-1-4020-4333-8_1.
(8) Odom, T. W.; Schatz, G. C. Introduction to Plasmonics. *Chem. Rev.* **2011**, *111* (6), 3667−3668.
(9) Kamat, P. V.; Hartland, G. V. Plasmons for Energy Conversion. *ACS Energy Lett.* **2018**, *3* (6), 1467−1469.
(10) Butt, M. A.; Khonina, S. N.; Kazanskiy, N. L. Plasmonics: A Necessity in the Field of Sensing-A Review (Invited). *Fiber and Integrated Optics* **2021**, *40* (1), 14−47.
(11) A Small World Full of Opportunities. *Nat. Mater.* **2010**, *9* (3), 181−181. .
(12) Stockman, M. I.; Kneipp, K.; Bozhevolnyi, S. I.; Saha, S.; Dutta, A.; Ndukaife, J.; Kinsey, N.; Reddy, H.; Guler, U.; Shalaev, V. M.; Boltasseva, A.; Gholipour, B.; Krishnamoorthy, H. N. S.; MacDonald, K. F.; Soci, C.; Zheludev, N. I.; Savinov, V.; Singh, R.; Groß, P.; Lienau, C.; Vadai, M.; Solomon, M. L.; Barton, D. R.; Lawrence, M.; Dionne, J. A.; Boriskina, S. V.; Esteban, R.; Aizpurua, J.; Zhang, X.; Yang, S.; Wang, D.; Wang, W.; Odom, T. W.; Accanto, N.; de Roque, P. M.; Hancu, I. M.; Piatkowski, L.; van Hulst, N. F.; Kling, M. F. Roadmap on Plasmonics. *J. Opt.* **2018**, *20* (4), 043001.
(13) Kuznetsov, A. I.; Miroshnichenko, A. E.; Fu, Y. H.; Zhang, J.; Luk'yanchuk, B. Magnetic Light. *Sci. Rep* **2012**, *2* (1), 492.
(14) Liu, W.; Kivshar, Y. S. Generalized Kerker Effects in Nanophotonics and Meta-Optics. *Opt. Express* **2018**, *26* (10), 13085.
(15) Person, S.; Jain, M.; Lapin, Z.; Sáenz, J. J.; Wicks, G.; Novotny, L. Demonstration of Zero Optical Backscattering from Single Nanoparticles. *Nano Lett.* **2013**, *13* (4), 1806−1809.
(16) Wray, P. R.; Atwater, H. A. Light−Matter Interactions in Films of Randomly Distributed Unidirectionally Scattering Dielectric Nanoparticles. *ACS Photonics* **2020**, *7* (8), 2105−2114.
(17) Babicheva, V. E.; Evlyukhin, A. B. Metasurfaces with Electric Quadrupole and Magnetic Dipole Resonant Coupling. *ACS Photonics* **2018**, *5* (5), 2022−2033.
(18) Babicheva, V. E.; Moloney, J. V. Lattice Effect Influence on the Electric and Magnetic Dipole Resonance Overlap in a Disk Array. *Nanophotonics* **2018**, *7* (10), 1663−1668.
(19) Bakker, R. M.; Permyakov, D.; Yu, Y. F.; Markovich, D.; Paniagua-Domínguez, R.; Gonzaga, L.; Samusev, A.; Kivshar, Y.; Luk'yanchuk, B.; Kuznetsov, A. I. Magnetic and Electric Hotspots with Silicon Nanodimers. *Nano Lett.* **2015**, *15* (3), 2137−2142.
(20) Geffrin, J. M.; García-Cámara, B.; Gómez-Medina, R.; Albella, P.; Froufe-Pérez, L. S.; Eyraud, C.; Litman, A.; Vaillon, R.; González, F.; Nieto-Vesperinas, M.; Sáenz, J. J.; Moreno, F. Magnetic and Electric Coherence in Forward- and Back-Scattered Electromagnetic Waves by a Single Dielectric Subwavelength Sphere. *Nat. Commun.* **2012**, *3*, 1171.
(21) Kruk, S.; Kivshar, Y. Functional Meta-Optics and Nanophotonics Governed by Mie Resonances. *ACS Photonics* **2017**, *4* (11), 2638−2649.
(22) Sautter, J.; Staude, I.; Decker, M.; Rusak, E.; Neshev, D. N.; Brener, I.; Kivshar, Y. S. Active Tuning of All-Dielectric Metasurfaces. *ACS Nano* **2015**, *9* (4), 4308−4315.
(23) Kivshar, Y.; Miroshnichenko, A. Meta-Optics with Mie Resonances. *Optics and Photonics News* **2017**, *28* (1), 24−31.
(24) Moitra, P.; Slovick, B. A.; li, W.; Kravchencko, I. I.; Briggs, D. P.; Krishnamurthy, S.; Valentine, J. Large-Scale All-Dielectric Metamaterial Perfect Reflectors. *ACS Photonics* **2015**, *2* (6), 692−698.
(25) Yang, C.-Y.; Yang, J.-H.; Yang, Z.-Y.; Zhou, Z.-X.; Sun, M.-G.; Babicheva, V. E.; Chen, K.-P. Nonradiating Silicon Nanoantenna Metasurfaces as Narrowband Absorbers. *ACS Photonics* **2018**, *5* (7), 2596−2601.
(26) Spinelli, P.; Verschuuren, M. A.; Polman, A. Broadband Omnidirectional Antireflection Coating Based on Subwavelength Surface Mie Resonators. *Nat. Commun.* **2012**, *3* (1), 692.
(27) Fu, Y. H.; Kuznetsov, A. I.; Miroshnichenko, A. E.; Yu, Y. F.; Luk'yanchuk, B. Directional Visible Light Scattering by Silicon Nanoparticles. *Nat. Commun.* **2013**, *4* (1), 1527.
(28) Evlyukhin, A. B.; Novikov, S. M.; Zywietz, U.; Eriksen, R. L.; Reinhardt, C.; Bozhevolnyi, S. I.; Chichkov, B. N. Demonstration of Magnetic Dipole Resonances of Dielectric Nanospheres in the Visible Region. *Nano Lett.* **2012**, *12* (7), 3749−3755.
(29) Babicheva, V. E.; Evlyukhin, A. B. Resonant Lattice Kerker Effect in Metasurfaces With Electric and Magnetic Optical Responses. *Laser & Photonics Reviews* **2017**, *11* (6), 1700132.
(30) García-Etxarri, A.; Gómez-Medina, R.; Froufe-Pérez, L. S.; López, C.; Chantada, L.; Scheffold, F.; Aizpurua, J.; Nieto-Vesperinas, M.; Sáenz, J. J. Strong Magnetic Response of Submicron Silicon Particles in the Infrared. *Opt. Express* **2011**, *19* (6), 4815.
(31) Ghadarghadr, S.; Mosallaei, H. Coupled Dielectric Nanoparticles Manipulating Metamaterials Optical Characteristics. *IEEE Transactions on Nanotechnology* **2009**, *8* (5), 582−594.
(32) Hopkins, B.; Filonov, D. S.; Miroshnichenko, A. E.; Monticone, F.; Alù, A.; Kivshar, Y. S. Interplay of Magnetic Responses in All-Dielectric Oligomers To Realize Magnetic Fano Resonances. *ACS Photonics* **2015**, *2* (6), 724−729.
(33) Miroshnichenko, A. E.; Kivshar, Y. S. Fano Resonances in All-Dielectric Oligomers. *Nano Lett.* **2012**, *12* (12), 6459−6463.
(34) Zywietz, U.; Schmidt, M. K.; Evlyukhin, A. B.; Reinhardt, C.; Aizpurua, J.; Chichkov, B. N. Electromagnetic Resonances of Silicon Nanoparticle Dimers in the Visible. *ACS Photonics* **2015**, *2* (7), 913−920.
(35) Cross, G. H. Fundamental Limit to the Use of Effective Medium Theories in Optics. *Opt. Lett., OL* **2013**, *38* (16), 3057−3060.
(36) Markel, V. Introduction to the Maxwell Garnett Approximation: Tutorial. *Journal of the Optical Society of America. A Optics, Image Science, and Vision* **2016**, *33* (7), 1244−1256.
(37) Niklasson, G. A.; Granqvist, C. G.; Hunderi, O. Effective Medium Models for the Optical Properties of Inhomogeneous Materials. *Appl. Opt.* **1981**, *20* (1), 26.
(38) Shivola, A. H. Self-Consistency Aspects of Dielectric Mixing Theories. *IEEE Transactions on Geoscience and Remote Sensing* **1989**, *27* (4), 403−415.

(39) Shalaev, V. M. *Nonlinear Optics of Random Media: Fractal Composites and Metal-Dielectric Films*; Springer Tracts in Modern Physics; Springer: Berlin, 2007.
(40) Fazio, B.; Artoni, P.; Antonia Iatì, M.; D'Andrea, C.; Lo Faro, M. J.; Del Sorbo, S.; Pirotta, S.; Giuseppe Gucciardi, P.; Musumeci, P.; Salvatore Vasi, C.; Saija, R.; Galli, M.; Priolo, F.; Irrera, A. Strongly Enhanced Light Trapping in a Two-Dimensional Silicon Nanowire Random Fractal Array. *Light Sci. Appl.* **2016**, *5* (4), e16062−e16062.
(41) Ball, P. Fractal Standstill. *Nat. Mater.* **2010**, *9* (12), 964−964.
(42) Stockman, M. I.; Pandey, L. N.; Muratov, L. S.; George, T. F. Giant Fluctuations of Local Optical Fields in Fractal Clusters. *Phys. Rev. Lett.* **1994**, *72* (15), 2486−2489.
(43) Liu, F.; Smallwood, G. J. Effect of Aggregation on the Absorption Cross-Section of Fractal Soot Aggregates and Its Impact on LII Modelling. *Journal of Quantitative Spectroscopy and Radiative Transfer* **2010**, *111* (2), 302−308.
(44) Karpov, S. V.; Gerasimov, V. S.; Isaev, I. L.; Markel, V. A. Local Anisotropy and Giant Enhancement of Local Electromagnetic Fields in Fractal Aggregates of Metal Nanoparticles. *Phys. Rev. B* **2005**, *72* (20), 205425.
(45) Kortshagen, U. R.; Sankaran, R. M.; Pereira, R. N.; Girshick, S. L.; Wu, J. J.; Aydil, E. S. Nonthermal Plasma Synthesis of Nanocrystals: Fundamental Principles, Materials, and Applications. *Chem. Rev.* **2016**, *116* (18), 11061−11127.
(46) Kramer, N. J.; Anthony, R. J.; Mamunuru, M.; Aydil, E. S.; Kortshagen, U. R. Plasma-Induced Crystallization of Silicon Nanoparticles. *J. Phys. D: Appl. Phys.* **2014**, *47* (7), 075202.
(47) Mangolini, L.; Thimsen, E.; Kortshagen, U. High-Yield Plasma Synthesis of Luminescent Silicon Nanocrystals. *Nano Lett.* **2005**, *5* (4), 655−659.
(48) Alvarez Barragan, A.; Ilawe, N. V.; Zhong, L.; Wong, B. M.; Mangolini, L. A Non-Thermal Plasma Route to Plasmonic TiN Nanoparticles. *J. Phys. Chem. C* **2017**, *121* (4), 2316−2322.
(49) Ho, A.; Mandal, R.; Lunt, R. R.; Anthony, R. J. Nonthermal Plasma Synthesis of Gallium Nitride Nanoparticles: Implications for Optical and Electronic Applications. *ACS Appl. Nano Mater.* **2021**, *4* (6), 5624−5629.
(50) Exarhos, S.; Alvarez-Barragan, A.; Aytan, E.; Balandin, A. A.; Mangolini, L. Plasmonic Core−Shell Zirconium Nitride−Silicon Oxynitride Nanoparticles. *ACS Energy Lett.* **2018**, *3* (10), 2349−2356.
(51) Choi, S. J.; Kushner, M. J. A Particle-in-Cell Simulation of Dust Charging and Shielding in Low Pressure Glow Discharges. *IEEE Trans. Plasma Sci.* **1994**, *22* (2), 138−150.
(52) Goree, J. Ion Trapping by a Charged Dust Grain in a Plasma. *Phys. Rev. Lett.* **1992**, *69* (2), 277−280.
(53) Matsoukas, T.; Russell, M. Particle Charging in Low-pressure Plasmas. *J. Appl. Phys.* **1995**, *77* (9), 4285−4292.
(54) Kortshagen, U.; Bhandarkar, U. Modeling of Particulate Coagulation in Low Pressure Plasmas. *Phys. Rev. E* **1999**, *60* (1), 887−898.
(55) Schweigert, V. A.; Schweigert, I. V. Coagulation in a Low-Temperature Plasma. *J. Phys. D: Appl. Phys.* **1996**, *29* (3), 655−659.
(56) Rao, N. P.; Lee, H. J.; Kelkar, M.; Hansen, D. J.; Heberlein, J. V. R.; McMurry, P. H.; Girshick, S. L. Nanostructured Materials Production by Hypersonic Plasma Particle Deposition. *Nanostructured Materials* **1997**, *9* (1−8), 129−132.
(57) Holman, Z. C.; Kortshagen, U. R. A Flexible Method for Depositing Dense Nanocrystal Thin Films: Impaction of Germanium Nanocrystals. *Nanotechnology* **2010**, *21* (33), 335302.
(58) Firth, P.; Holman, Z. C. Aerosol Impaction-Driven Assembly System for the Production of Uniform Nanoparticle Thin Films with Independently Tunable Thickness and Porosity. *ACS Appl. Nano Mater.* **2018**, *1* (8), 4351−4357.
(59) Bapat, A.; Anderson, C.; Perrey, C. R.; Carter, C. B.; Campbell, S. A.; Kortshagen, U. Plasma Synthesis of Single-Crystal Silicon Nanoparticles for Novel Electronic Device Applications. *Plasma Phys. Control. Fusion* **2004**, *46* (12B), B97−B109.
(60) Markel, V. A.; Shalaev, V. M.; Poliakov, E. Y.; George, T. F. Fluctuations of Light Scattered by Fractal Clusters. *J. Opt. Soc. Am. A* **1997**, *14* (1), 60.
(61) Botet, R.; Rannou, P.; Cabane, M. Mean-Field Approximation of Mie Scattering by Fractal Aggregates of Identical Spheres. *Appl. Opt.* **1997**, *36* (33), 8791.
(62) Farias, T. L.; Köylü, Ü. Ö.; Carvalho, M. G. Range of Validity of the Rayleigh−Debye−Gans Theory for Optics of Fractal Aggregates. *Appl. Opt.* **1996**, *35* (33), 6560.
(63) Perrin, J.-M.; Lamy, P. L. On the Validity of Effective-Medium Theories in the Case of Light Extinction by Inhomogeneous Dust Particles. *Astrophysical Journal* **1990**, *364*, 146.
(64) Videen, G.; Chýlek, P. Scattering by a Composite Sphere with an Absorbing Inclusion and Effective Medium Approximations. *Opt. Commun.* **1998**, *158* (1), 1−6.
(65) Voshchinnikov, N. V.; Videen, G.; Henning, T. Effective Medium Theories for Irregular Fluffy Structures: Aggregation of Small Particles. *Appl. Opt.* **2007**, *46* (19), 4065.
(66) Wang, G.; Sorensen, C. M. Experimental Test of the Rayleigh-Debye-Gans Theory for Light Scattering by Fractal Aggregates. *Appl. Opt.* **2002**, *41* (22), 4645.
(67) Smith, D. R.; Vier, D. C.; Koschny, Th.; Soukoulis, C. M. Electromagnetic Parameter Retrieval from Inhomogeneous Metamaterials. *Phys. Rev. E* **2005**, *71* (3), 036617.
(68) Barrera, R. G.; García-Valenzuela, A. Coherent Reflectance in a System of Random Mie Scatterers and Its Relation to the Effective-Medium Approach. *J. Opt. Soc. Am. A* **2003**, *20* (2), 296.
(69) Bapat, A.; Gatti, M.; Ding, Y.-P.; Campbell, S. A.; Kortshagen, U. A Plasma Process for the Synthesis of Cubic-Shaped Silicon Nanocrystals for Nanoelectronic Devices. *J. Phys. D: Appl. Phys.* **2007**, *40* (8), 2247−2257.
(70) Barabási, A. L.; Stanley, H. E. *Fractal Concepts in Surface Growth*; Cambridge University Press, 1995.
(71) Dick, V. V.; Solov'yov, I. A.; Solov'yov, A. V. Nanoparticles Dynamics on a Surface: Fractal Pattern Formation and Fragmentation. *Journal of Physics: Conference Series* **2010**, *248*, 012025.
(72) Heinson, W. R. Simulation Studies on Shape and Growth Kinetics for Fractal Aggregates in Aerosol and Collodial Systems. Doctoral dissertation, Kansas State University, 2008, p 126.
(73) Mackowski, D. The Extension of Mie Theory to Multiple Spheres. In *The Mie Theory: Basics and Applications*; Hergert, W., Wriedt, T., Eds.; *Springer Series in Optical Sciences*; Springer: Berlin, Heidelberg, 2012; pp 223−256. DOI: 10.1007/978-3-642-28738-1_8.
(74) T-Matrix Theory of Electromagnetic Scattering by Partciles and Its Applications: A Comprehensive Reference Database. *Journal of Quantitative Spectroscopy and Radiative Transfer* **2004**, *88* (1−3), 357−406. .
(75) Egel, A.; Czajkowski, K. M.; Theobald, D.; Ladutenko, K.; Kuznetsov, A. S.; Pattelli, L. SMUTHI: A Python Package for the Simulation of Light Scattering by Multiple Particles near or between Planar Interfaces. *Journal of Quantitative Spectroscopy and Radiative Transfer* **2021**, *273*, 107846.
(76) Doicu, A.; Wriedt, T.; Eremin, Y. A. *Light Scattering by Systems of Particles: Null-Field Method with Discrete Sources: Theory and Programs*; Springer Series in Optical Sciences; Springer-Verlag: Berlin, 2006. DOI: 10.1007/978-3-540-33697-6.
(77) Cruzan, O. R. Translational Addition Theorems for Spherical Vector Wave Functions. *Quarterly of Applied Mathematics* **1962**, *20* (1), 33−40.
(78) Kahnert, F. M. Numerical Methods in Electromagnetic Scattering Theory. *Journal of Quantitative Spectroscopy and Radiative Transfer* **2003**, *79* (80), 775−824.
(79) Waterman, P. C. Matrix Formulation of Electromagnetic Scattering. *Proceedings of the IEEE* **1965**, *53* (8), 805−812.
(80) Mühlig, S.; Menzel, C.; Rockstuhl, C.; Lederer, F. Multipole Analysis of Meta-Atoms. *Metamaterials* **2011**, *5* (2−3), 64−73.

(81) Yuffa, A. J.; Scales, J. A. Object-Oriented Electrodynamic S-Matrix Code with Modern Applications. *J. Comput. Phys.* **2012**, *231* (14), 4823−4835.
(82) Mackowski, D. W. Calculation of Total Cross Sections of Multiple-Sphere Clusters. *J. Opt. Soc. Am. A* **1994**, *11* (11), 2851.
(83) Xiong, Z.; Lanham, S.; Husmann, E.; Nelson, G.; Eslamisaray, M. A.; Polito, J.; Liu, Y.; Goree, J.; Thimsen, E.; Kushner, M. J.; Kortshagen, U. R. Particle Trapping, Size-Filtering, and Focusing in the Nonthermal Plasma Synthesis of Sub-10 Nanometer Particles. *J. Phys. D: Appl. Phys.* **2022**, *55* (23), 235202.

https://doi.org/10.1021/acsami.2c03263
ACS Appl. Mater. Interfaces 2022, 14, 23624−23636